Journal of
Materials Chemistry C

Materials for optical, magnetic and electronic devices

rsc.li/materials-c

Themed issue: Materials for molecular electronics and magnetism

ROYAL SOCIETY
OF CHEMISTRY

PAPER
Keiichi Katoh, Ryo Nakanishi, Masahiro Yamashita *et al.*
Terbium(III) bis-phthalocyaninato single-molecule magnet
encapsulated in a single-walled carbon nanotube

Terbium(III) bis-phthalocyaninato single-molecule magnet encapsulated in a single-walled carbon nanotube†

Keiichi Katoh, [ID] *[a] Junya Sato,[b] Ryo Nakanishi,*[b] Ferdous Ara, [ID] [c] Tadahiro Komeda, [ID] [c] Yuki Kuwahara,[d] Takeshi Saito, [ID] [d] Brian K. Breedlove[b] and Masahiro Yamashita*[be]

In this study, terbium(III) bis-phthalocyaninato single-molecule magnets (TbPc$_2$ SMMs) were encapsulated in the internal nano space of single-walled carbon nanotubes (SWCNTs) for the first time. The magnetic and electronic properties of the TbPc$_2$ SMM–SWCNT hybrids were investigated in detail by using dc and ac magnetic susceptibility measurements, TEM, SEM, STM, STS, *etc.* By arranging the TbPc$_2$ SMMs in the one-dimensional internal nano spaces of SWCNTs, it is possible to investigate the essential SMM characteristics of TbPc$_2$ without considering ligand field (LF) effects. In addition, it appears that the electron correlation between TbPc$_2$ and the SWCNT can affect the electrotransport and/or electromagnetic properties. Furthermore, since the stable internal nano space of SWCNTs is used, it is thought that the density of SMMs in the SMM–SWCNT hybrid material can be controlled, and the hybrids should be usable as spin valves. Our strategy may pave the way for the construction of SMM–SWCNT hybrid materials.

Introduction

It is no exaggeration to say that modern society is supported by highly functional materials, especially those containing magnets based on nanoscale units. Improving molecular electronics, spintronics, data storage and quantum information processing is important for the further development of an information-oriented society in the future.[1–7] In recent years, single-molecule magnets (SMMs) have been prepared as metal complexes by using bottom-up methods.[1,8–14] These SMMs exhibit slow magnetic relaxation behaviour with magnetic hysteresis at extremely low temperatures, magnetic bistabilities, quantum tunnelling of the magnetization, and quantum coherence. In 1993, Sessoli and Gatteschi *et al.* reported the first example of an

SMM, $[Mn_{12}O_{12}(OAc)_{16}(H_2O)_4] \cdot 2AcOH$ (abbreviated as Mn_{12}).[8,15] Classical magnets exhibit large magnetization *via* three-dimensional interactions of the electron spins of the metal ions, but for SMMs, uniaxial magnetic anisotropy of one molecule occurs. For SMMs, the degeneracy of the total spin state S is split into $(2S + 1)$ by the ligand field (LF), and double-well potentials occur for the spin sublevel, causing a barrier to spin relaxation. At this time, the split width of the energy levels is defined as $U_{eff} = |D|S^2$ (D = zero-field splitting constant) (*e.g.*, for Mn_{12}, $D = -0.46$ cm^{-1}, $S = 10$, $U_{eff} = 40$ cm^{-1} and coercivity (H_C) = 2.2 T@1.5 K) due to the magnetic anisotropy. At low temperatures, SMMs behave like magnets which undergo slow magnetic relaxation. On the other hand, the lanthanoid-type SMMs are different from transition metal SMMs since their SMM behaviours come from the f electrons. Since the orbital angular momentum L does not disappear for f electrons, ground multiplets having a total angular momentum, J, form due to spin–orbit interactions. When the ground multiplet is placed in an LF environment, the degeneration splits into $(2J + 1)$ sublevels. As a result, double-well potentials form, and SMM behaviour is exhibited.[8,16] In general, the sublevel splitting in lanthanoid-type SMMs (10^2–10^3 cm^{-1})[17] is much larger than that of transition metal-type SMMs (*ca.* 70 cm^{-1}),[18] meaning that Ln type SMMs are more useful in terms of SMM characteristics, such as U_{eff}.[19] Here we focused on a terbium(III) phthalocyaninato double-decker SMM. In 2003, anionic $[TbPc_2]^- \cdot TBA^+$ (Tb^{3+} = terbium(III) ion, Pc^{2-} = phthalocyaninato, TBA$^+$ = (C$_4$H$_9$)$_4$N$^+$) was reported as the first single ion

[a] Department of Chemistry, Graduate School of Science, Josai University, 1-1 Keyakidai, Sakado, Saitama 350-0295, Japan. E-mail: kkatoh@josai.ac.jp

[b] Department of Chemistry, Graduate School of Science, Tohoku University, 6-3 Aramaki Aza Aoba, Aoba-ku, Sendai 980-8578, Japan

[c] Institute of Multidisciplinary Research of Advanced Materials, Tohoku University, 2-1-1, Katahira, Aoba-ku, Sendai 980-0877, Japan

[d] National Institute of Advanced Industrial Science and Technology (AIST), Tsukuba 305-8565, Japan

[e] School of Materials Science and Engineering, Nankai University, Tianjin 300350, China

† Electronic supplementary information (ESI) available. See DOI: 10.1039/d1tc01026c

This journal is © The Royal Society of Chemistry 2021

J. Mater. Chem. C, 2021, **9**, 10697–10704 | **10697**

magnet (SIM) by Ishikawa *et al.* (U_{eff} = 230 cm^{-1}, $H_C \approx$ 0.01 T@0.04 K),[16,20] and in the following year, the same group reported neutral TbPc$_2$ in which the π-radical were delocalized on the Pc^{2-} ligands (Pc$^{\bullet-}$).[21] The peak-top temperature of χ″ for TbPc$_2$ at an alternating current (ac) frequency of 1500 Hz (ν) has been reported to be about 50 K (U_{eff} = 410 cm^{-1}), which is high compared to Mn$_{12}$ SMMs. However, butterfly-type magnetic hysteresis is observed below 1.8 K. This magnetic behaviour is due to the magnetic relaxation *via* quantum tunnelling of the magnetization (QTM). If QTM is suppressed, magnetic hysteresis with H_C can be observed at temperatures much higher than those of conventional SMMs.[22] From the viewpoint of suppressing QTM, we were able to suppress QTM and improve the H_C of TbPc$_2$ derivatives by utilizing the magnetic dipole interactions between SMMs. A one-dimensional structure was confirmed for TbNcPc in which naphthalocyaninato (Nc^{2-}) and Pc^{2-} are coordinated to the Tb^{3+} ion, and magnetic hysteresis with H_C was observed at a relatively high temperature of 25 K (U_{eff} = 584 cm^{-1}, $H_C \approx$ 150 mT@1.8 K).[23] In other words, the magnetic hysteresis properties were improved by suppressing QTM. In addition, we have compared the SMM properties of crystal samples of TbPc$_2$ ($P2_12_12_1$, P_{nma}) and magnetically diluted TbPc$_2$ samples.[24] Diluting the γ-phase ($P2_12_12_1$) causes the hysteresis loop in the magnetization (*M*) *versus* magnetic field (*H*) to open. In other words, the SMM characteristics are improved. On the other hand, for the P_{nma} crystal, the *M*–*H* hysteresis loop is open. Thus, for TbPc$_2$, the combination of the orientation of the magnetic anisotropy and the arrangement of the magnetic dipole interactions has a dramatic effect on the performance of SMMs. In order to design SMMs for practical use, U_{eff} must be increased, and fast QTM processes must be suppressed.

In addition, the internal nano space of carbon nanotubes (CNTs) can be regarded as reaction vessels, which are 1/1000 smaller than that of a microreactor.[25] Therefore, a chemical reaction field on a diameter range of 1–3 nm (100 nm to 0.1 mm in length) is expected to have a great influence on reaction chemistry and/or nanoelectronics research in the 21st century.[26–29] It has been shown that atoms and molecules can be contained in the nano space of CNTs.[30–35] Focusing on the use of the stable one-dimensional nano space of a CNT as a host for host–guest structures, various SMM–CNT hybrid materials have been reported for nanoelectronics and spintronics research.[36] In 2011, Del Carmen Giménez-López *et al.* reported Mn$_{12}$@MWCNT, where Mn$_{12}$ with a diameter of 1.6 nm and a height of 1.1 nm was incorporated in a multi-walled CNT (MWCNT) (internal diameter range 5–50 nm), and its magnetic properties.[37] It shows that the SMM characteristics decrease after encapsulation in MWCNTs. In 2017, we encapsulated Dy(acac)$_3$(H$_2$O)$_2$ SMMs in MWCNTs by using a capillary method (abbreviated Dy(acac)$_3$(H$_2$O)$_2$@MWCNT).[38] Dy(acac)$_3$(H$_2$O)$_2$@MWCNT shows clear ac frequency dependence, but it does not have enhanced SMM properties. In 2009, Kyatskaya *et al.* reported a TbPc$_2$–SWCNT hybrid material, where a TbPc$_2$ derivative was attached to the outside of a SWCNT, and its magnetic properties.[39] In TbPc$_2$–SWCNT hybrid spin valves, the maximum magnetic resistance ratio between the parallel state and the antiparallel state is about 300% at submillikelvin temperatures.[40]
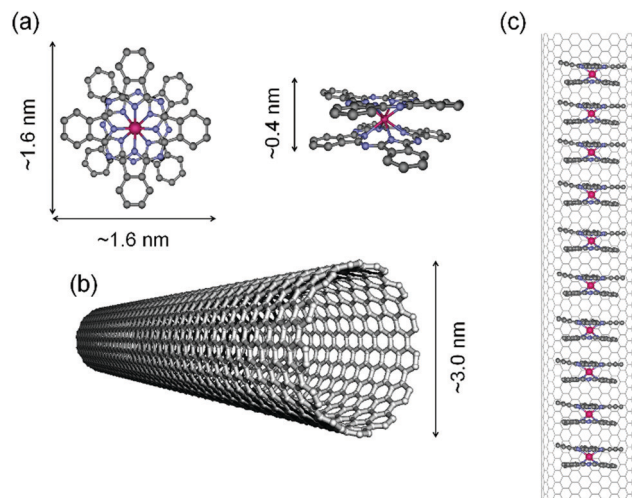

Fig. 1 Chemical structure of TbPc$_2$ SMM and schematic illustration of its encapsulation in SWCNTs. (a) Ball and stick structure of TbPc$_2$. Hydrogen atoms omitted for clarity: top (left) and side (right) view. Colouring scheme: Tb^{3+}, pink; N, cyan; C, grey. (b) Ball and stick structure of SWCNTs. (c) Schematic illustration of the TbPc$_2$ SMM encapsulated in a SWCNTs (abbreviated as TbPc$_2$@SWCNT).

It suggests that a spin valve with a larger magnetoresistance ratio can be prepared by using SMMs instead of ferromagnets as the spin source. In 2018, we encapsulated DySc$_2$N@C$_{80}$ SMMs in SWCNT nano-peapods (abbreviated DySc$_2$N@C$_{80}$@SWCNT) and reported on the magnetic properties.[41] From a magnetization (*M*) *vs.* magnetic field (*H*) plot at 1.8 K, a significant improvement in H_C was observed after encapsulation in a SWCNT. The improvement in the magnetic properties is thought to be due to the following two factors. First, the one-dimensional chain structure of DySc$_2$N@C$_{80}$ in a SWCNT works on the magnetic dipole interactions between adjacent DySc$_2$N@C$_{80}$ molecules, and the dipolar bias suppresses the magnetic relaxation of QTM. Second, charge transfer (CT) between DySc$_2$N@C$_{80}$ and SWCNT causes perturbations in the crystal field (CF).

Inspired by the previous research, we investigated whether or not QTM could be suppressed using the dipolar bias associated with the one-dimensional TbPc$_2$ SMM chain structure in the internal space of SWCNTs. In addition, since the stable nano space of SWCNTs allows the control of the arrangement of SMMs, detailed investigation of the role of the SMM sequence in spin valve characteristics may be possible. To the best of our knowledge, no examples of TbPc$_2$ SMM encapsulated in a SWCNT have been reported to date. Finally, we investigated the effects of CT and LF (or CF) distortions on the magnetic properties of TbPc$_2$ SMMs encapsulated in the nano space of SWCNTs. If we can take advantage of the TbPc$_2$ SMM characteristics in a SWCNT, highly functional materials can be prepared (Fig. 1).

Experimental

General procedure for the synthesis of TbPc$_2$

All reagents were purchased from Wako Pure Chemical Industries, Ltd, TCI, Strem Chemicals, Inc. and Sigma-Aldrich Co.

LLC. and used without further purification. TbPc$_2$ was prepared following a reported procedure.[42] A mixture of 1,2-dicyanobenzene (62.7 mmol), Tb(OAc)$_3$·4H$_2$O (3.92 mmol) and 1,8-diazabicyclo [5,4,0]undec-7-ene (DBU) (33.5 mmol) in 40 mL of 1-hexanol was refluxed for 42 h. The solution was allowed to cool to room temperature and then filtered. The precipitate was washed with *n*-hexane. Then the precipitate was dried in air. The crude purple product was extracted with ten 200 mL portions of CHCl$_3$. The green extracts were combined, concentrated, and purified using column chromatography (C-200 silica gel, Wako). The eluent was 98:2 CH$_2$Cl$_2$/MeOH. The green fraction, which was the first fraction, was collected while being careful not to contaminate with the anionic [TbPc$_2$]$^-$ complex, which was the second fraction (blue-green). The green fraction was concentrated, and *n*-hexane was added until the compound precipitated. The green precipitate was filtered and dried *in vacuo*. The solid (8 mg) was dissolved in 20 mL of CHCl$_3$ and filtered. *n*-Hexane was layered on the top of green filtrate. After two weeks, deep green needle-like crystals were obtained in the γ-phase (Fig. S1, ESI†).[42] In general TbPc$_2$ exhibits two broad absorption bands characteristic of a radical Pc$^{•-}$ ligand in the ranges of 450–500 nm (BV: Blue Vibronic) and 900–1000 nm (RV: Red Vibronic) as well as another broad band in the range of 1200–2000 nm due to intramolecular CT (IV: Intervalence Transition) between the two rings (Fig. S2, ESI†).[43] In the spectra, only four main absorption bands in the UV-visible region were observed. The three main absorption bands were assigned to the Q (670 and 600 nm) and Soret bands (320 nm). TbPc$_2$ was then encapsulated in a SWCNT of without further purification. ESI-MS: *m/z* (%): 1183.22423 (100%) [M$^+$] (calcd 1183.22493).

Procedures for the encapsulation of TbPc$_2$ in SWCNTs

In order to encapsulate TbPc$_2$ with a diameter of 1.6 nm and a height of 0.4 nm in a SWCNT, SWCNTs with an average diameter of 2.4 ± 0.6 nm, which were synthesized by using enhanced direct injection pyrolytic synthesis (eDIPS) method, were used.[44,45] The SWCNTs were cleaned as follows: The SWCNTs (29.8 mg) were heated in an electric furnace at 550 °C in air for 30 min to remove the carbon shell covering the metal catalyst. Next, the sample was dispersed in 75 mL of a prepared 2% hexadecyltrimethylammonium bromide aqueous solution for 24 h using an additive to remove the metals and metal oxides contained in the SWCNTs, and the mixture was heated in a 300 mL round-bottom flask at 100 °C for 5 days. Then the SWCNTs were collected by using filtration with a membrane filter made of hydrophilic polytetrafluoroethylene and having a pore size of 1 μm. The SWCNTs were dispersed in 50 mL of methanol, and filtration was repeated 3 times. The SWCNTs were placed in an electric furnace and vacuum heated at 1200 °C for 24 h to remove unreacted metals. The yield was 18.7 mg. In Fig. S3 (ESI†), scanning electron microscope (SEM) images before and after cleaning and a transmission electron microscope (TEM) image of the SWCNTs after cleaning are shown together with elemental analysis obtained by using energy dispersive X-ray (EDX) spectrometry. From the results of elemental analysis, the peak derived from Fe, which was used as a catalyst in the synthesis of the SWCNTs, which was present

before cleaning, was absent after cleaning. In addition, no peaks indicating impurities were observed in the EDX spectra, but it was not confirmed using TEM that the internal space of the SWCNTs did not contain impurities. In other words, the catalyst was not completely removed using the cleaning procedures (please see the Magnetic properties section).

TbPc$_2$ was encapsulated into SWCNTs (hereinafter abbreviated as TbPc$_2$@SWCNT) using a capillary method as follows. One end of the SWCNT was opened by heating the SWCNTs (18.7 mg) in air at 550 °C for 30 min in a glass tube and then vacuum-heated with a gas burner to remove impurities from the SWCNTs. Next, the synthesized TbPc$_2$ (5.2 mg, 5.0 mg, and 4.9 mg) was placed in three 30 mL sample tubes, 25 mL of methanol was added to each sample tube, and the sample tubes were shaken using an ultrasonic cleaner. The above SWCNTs (7.2 mg, 5.5 mg, 4.4 mg, respectively) were added to the three tubes and dispersed. After 1 week, the samples were collected by filtration, washed with methanol and dried in a vacuum desiccator. The samples were placed in glass tubes, and then the tubes were heated under vacuum at 200 °C for 2 h. Next, three dispersions of C$_{60}$ (5 mg) in 25 mL of 1, 2-dichloroethane were added to the TbPc$_2$@SWCNT solutions (TbPc$_2$@SWCNT (mg):C$_{60}$ (mg) = 12.2:5.3, 9.6:4.8, 9.1:5.1), and allowed to disperse for 1 h. The ends of the SWCNTs were closed. The material was collected by using filtration, washed with 25 mL of toluene, 1,2-dichloroethane, and chloroform until the filtrate became colourless to remove C$_{60}$ and TbPc$_2$ on the surface. The product was dried in a vacuum desiccator. The yield was 27.4 mg.

Physical property measurements

Electrospray ionization mass (ESI) spectroscopy was performed at the Research and Analytical Centre for Giant Molecules, Tohoku University. UV-Vis-NIR spectra for solutions of TbPc$_2$ (1 × 10^{-5} mol dm^{-3}) in CHCl$_3$ in a quartz cell with a pathlength of 1 cm were acquired on a SHIMADZU UV-3100PC at 298 K. Powder X-ray diffraction patterns were collected on a Bruker D2 PHASER with Cu Kα radiation (λ = 1.5406 Å) at 298 K, a diffraction angle, 2θ, range of 5.0°–50.0°, a sampling width of 0.02°, and an irradiation time of 0.5 seconds. TbPc$_2$@SWCNT and SWCNTs were identified by using scanning electron microscopy (SEM), transmission electron microscopy (TEM), and energy dispersive X-ray (EDX) spectrometry. SEM images were acquired on a S-4300 manufactured by Hitachi High-Technologies Corporation. TEM and STEM images were acquired using a JEM-2100F manufactured by JEOL (acceleration voltage; 200 kV) and Titan cubed G2 60-300 manufactured by FEI (acceleration voltage; 60 kV). For TEM and STEM, the samples were prepared by dispersing the samples in 1, 2-dichloroethane then dropping them onto Cu grids, followed by heating in a vacuum. For scanning tunneling microscopy (STM), a solution of 1 mg of dry encapsulated SWCNTs in 5 mL of dichloroethane was mixed using an ultrasonicator (100 W) for 1 h. After sonication, the dispersion was drop-casted onto Au(111) substrates, which were flame-annealed in air prior to the deposition. After deposition, the sample was annealed

This journal is © The Royal Society of Chemistry 2021

J. Mater. Chem. C, 2021, **9**, 10697–10704 | **10699**

again in air at 200 °C for 2 h to evaporate the extra carbon and residuals. The samples were placed in an ultra-high vacuum (UHV) environment and STM and scanning tunneling spectroscopy (STS) measurements were conducted using a commercial low-temperature STM (Unisoku, Japan) with a base pressure of 10^{-8} Pa. All measurements were done in a constant current mode at ~ 4.6 K with an electrochemically etched W tip (Unisoku, Japan). A lock-in detection technique was used to acquire dI/dV curves. Gwyddion and Origin Pro were used to process the STM images and STS data.

Magnetic property measurements

Magnetic susceptibility measurements were performed on Quantum Design SQUID magnetometers MPMS-3 (Quantum Design, San Diego, CA, USA). Direct current (dc) measurements were performed in the temperature (T) range of 1.8–300 K and in dc magnetic fields (H_{dc}) of ±70 000 Oe. Alternating current (ac) measurements were performed in an ac frequency (ν) range of 1–1000 Hz with an ac field amplitude of 3 Oe in the presence of an H_{dc} of zero. Measurements were performed on randomly oriented powder samples of TbPc$_2$@SWCNT (26.9 mg), which were placed in gelatine capsules and fixed to prevent them from moving during measurements. Molar magnetic susceptibilities were not calculated because the content of TbPc$_2$ in the SWCNTs could not be estimated. In Fig. S4 (ESI†), the magnetic susceptibility of SWCNTs (18.68 mg) were determined from χ $vs.$ T plots. It is thought that the magnetic properties are due to magnetic impurities in SWCNTs. In the procedures for the encapsulation of TbPc$_2$ in the SWCNTs, described in the Experimental section, the Fe is used as a catalyst in the synthesis of the SWCNTs.[44,45] The presence of trace amounts of Fe, as iron oxide, was confirmed by using EDX after purification of the SWCNTs (Fig. S3, ESI†). The magnetic impurities could not be completely removed during the purification of the SWCNTs, which combined into fibre bundles. However, the magnetic susceptibilities (χ) of the SWCNTs are sufficiently smaller than those of TbPc$_2$@SWCNT (Fig. S7, ESI†). Moreover, no clear frequency dependence was observed in the ac measurements (Fig. S8-2, ESI†). Therefore, the effects of the magnetic impurities are negligible.

Results and discussion

Fig. 2 shows TEM images of TbPc$_2$@SWCNT and EDX and high-angle annular dark field scanning TEM (HAADF-STEM) images (Fig. S5, ESI†). From the TEM image, the internal space of SWCNT was empty before inclusion but contained something after encapsulation. In addition, from the EDX spectrum, a peak corresponding to the energy of the characteristic X-ray emitted from the Tb atom was confirmed. In addition, HAADF-STEM images showed white spots for Tb, indicating that TbPc$_2$ was encapsulated. In other words, some of the substances contained in the SWCNTs were TbPc$_2$ molecules, and TbPc$_2$@SWCNT was prepared. However, TbPc$_2$ is probably in a magnetic diluted state in the SWCNTs. From the STM image,
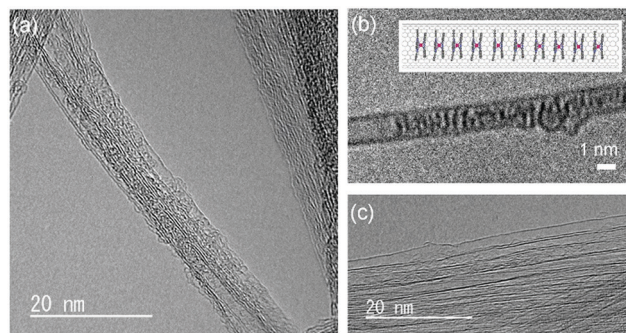

Fig. 2 Structural characterization of TbPc$_2$@SWCNT. Conventional bright field and phase contrast TEM images of TbPc$_2$ encapsulated in SWCNTs. (a) TbPc$_2$ was confirmed to be inside SWCNTs. Tb was detected by using EDX (see Fig. S3, ESI†). (b) TbPc$_2$ were partially stacked one-dimensionally in SWCNTs. (c) Empty SWCNT.

the vertical placement of the π-conjugated plane between TbPc$_2$ and the SWCNT is thought to be due to the presence of CH–π interactions. An X-ray photoelectron spectroscopy (XPS) spectrum of TbPc$_2$@SWCNT is shown in Fig. S6 (ESI†). Each peak was assigned as shown. The broad peak observed in the range of 1200–1300 cm^{-1} after inclusion was thought to be due to the Tb ion, but it was not confirmed. This is because the amounts of TbPc$_2$ and, thus, the Tb ions in the SWCNTs are relatively low. Furthermore, a peak due to N of phthalocyaninato ligands was observed in the XPS spectrum of TbPc$_2$@SWCNT. However, the amount of TbPc$_2$ molecules cannot be calculated from the intensity ratio of the N peak due to the influence of hexadecyl-trimethylammonium bromide used for cleaning the SWCNTs.

Fig. S7a (ESI†) shows the temperature dependence of the dc magnetic susceptibilities (χ) of TbPc$_2$@SWCNT at 1000 Oe. The rise in the χ values of TbPc$_2$@SWCNT at low temperature is thought to be from the spins of TbPc$_2$. In addition, there were no ferromagnetic interactions below 10 K from a χT $vs.$ T plot for TbPc$_2$@SWCNT (Fig. S7b, ESI†). It suggests that TbPc$_2$ is in a diluted state in the SWCNTs. Fig. 3 and Fig. S8 (ESI†) show the frequency (ν) and temperature (T) dependences of the ac magnetic susceptibilities of TbPc$_2$@SWCNT in a zero magnetic field. The ac frequency dependence of TbPc$_2$@SWCNT was confirmed. In a χ'' $vs.$ T plot, a peak top of T was observed in the range of 30–50 K, which is close to that of pristine TbPc$_2$. In other words, the magnetic relaxation behaviour in TbPc$_2$@SWCNT is not lost. Moreover, the peak temperature position was shifted to the lower temperature side in comparison to that of pristine TbPc$_2$ (Fig. S8, ESI†).[21] Since the shift resembles that for diluted samples of pristine TbPc$_2$, it is thought that TbPc$_2$ is in a diluted state in the SWCNTs. Detailed measurements of ac magnetic susceptibilities were performed to compare the SMM properties of TbPc$_2$ before and after encapsulation in SWCNTs. An Arrhenius plot for TbPc$_2$@SWCNT was prepared using the peak top temperature data in Fig. S9 (ESI†) using $\tau = \tau_0 \exp(U_{eff}/T)$ and $\tau = 1/(2\pi\nu)$ (Table S1, ESI†), and U_{eff} was estimated to be 430 cm^{-1} with the frequency factor (τ_0) $\approx 2.9 \times 10^{-10}$ s. This value is similar to that for pristine TbPc$_2$ ($U_{eff} \approx 410$ cm^{-1} with $\tau_0 \approx 1.5 \times 10^{-9}$ s).[21]
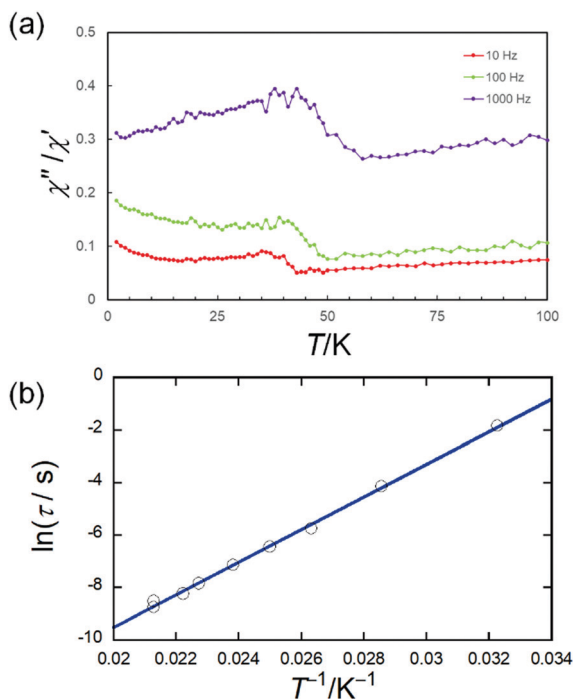
Fig. 3 Frequency (ν) and temperature (T) dependences of the ac magnetic susceptibilities (in-phase (χ'), out-of-phase (χ'')) of TbPc$_2$@SWCNT. (a) χ''/χ' versus T plot at the given ν (10, 100, 1000 Hz) of the ac susceptibility data (Fig. S8, ESI†). We have tried to clarify the existence of peaks by displaying the data as a χ''/χ' versus T plot because it is difficult to clearly determine the position of the peaks from χ'' vs. T plots (Fig. S8-1(b), ESI†). The lines are guides for eyes. In addition, the peak top position in the χ''/χ' versus T plot is the same as the peak top position in the χ'' vs. T plot (from ref. 21). (b) Arrhenius plots for TbPc$_2$@SWCNT, for which the τ values were obtained from Fig. S9 (ESI†).

The small difference is due to the dilution conditions. In addition, the U_{eff} and τ_0 values for TbPc$_2$–SWCNT hybrid material are on the same order of magnitude ($U_{\text{eff}} \approx 351$ cm^{-1} with $\tau_0 \approx 6.2 \times 10^{-8}$ s).[39]

Fig. 4 shows a plot of M vs. H for TbPc$_2$@SWCNT with slight butterfly-type magnetic hysteresis at 1.8 K. This M–H behaviour is similar to the magnetically diluted sample of TbPc$_2$.[24] Moreover, the magnetic hysteresis did not improve at high temperature. It is known that the magnetic hysteresis of TbPc$_2$ changes depending on the difference in the dimensionality of the intermolecular interactions.[24] Since TbPc$_2$ is in a diluted state in a SWCNT, i.e., the number of TbPc$_2$ molecules in the SWCNTs is small, the interactions between the molecules are suppressed. In the case of Mn$_{12}$@MWCNT, from the ac magnetic susceptibility measurements, it undergoes two different magnetic relaxation processes.[37] The authors conclude that there are two types of Mn$_{12}$ molecules with axes in different external environments, causing changes in the uniaxial magnetic anisotropy parameter D and the different magnetic relaxation processes. In addition, the U_{eff} obtained from the peak position of χ'' has been estimated to be 57 K, which is lower than the activation barrier ($U_{\text{eff}} = 72$ K) for pristine Mn$_{12}$.[15,37] For Mn$_{12}$@MWCNT, H_{C} is smaller than that for pristine Mn$_{12}$. Moreover, the changes in the derivatives of the hysteresis
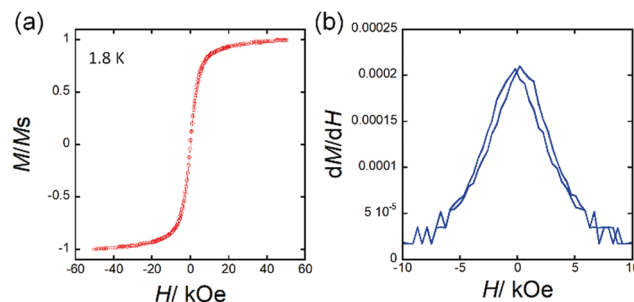

Fig. 4 (a) M–H curve and (b) dM/dH versus H plot for TbPc$_2$@SWCNT at 1.8 K. The vertical axis, M/M_s, shows magnetization values normalized to the saturated magnetization value. The butterfly-type magnetic hysteresis seems to be closed in (a), but it is slightly open which was confirmed by using magnetic field differentiation of M in (b). The lines are guides for eyes.

curves near a zero magnetic field increase, meaning that the magnetic relaxation via QTM is promoted. Therefore, they conclude that the SMM characteristics decrease after encapsulated in a MWCNT. In the case of DySc$_2$N@C$_{80}$@SWCNT, from field-cooled (FC) and zero field-cooled (ZFC) measurements, the blocking temperature ($T_B = 5$ K) does not change before and after encapsulation in a SWCNT.[41] On the other hand, from a M–H plot at 1.8 K, a significant improvement in H_{C} has been observed after encapsulation in SWCNTs. This is due to the following two factors. First, the one-dimensional chain structure of DySc$_2$N@C$_{80}$ in the SWCNT affects the magnetic dipole interactions between adjacent DySc$_2$N@C$_{80}$ molecules, and the dipolar bias suppresses QTM. Second, charge transfer (CT) between SWCNT and DySc$_2$N@C$_{80}$ may increase the magnetic moment. In a report in which DySc$_2$N@C$_{80}$ is included in MOF-177, the effective magnetic moment of DySc$_2$N@C$_{80}$@MOF-177 has been reported to increase due to the CT from MOF-177 to DySc$_2$N@C$_{80}$, and they conclude that CT perturbs the crystal field (CF) around the Dy^{3+} ion, suppresses QTM, and improves H_{C}.[46] In case of TbPc$_2$@SWCNT, LF of TbPc$_2$ was not perturbed. In other words, it is possible to investigate the essential SMM characteristics of TbPc$_2$ in the one-dimensional internal nano space of the SWCNTs without considering LF effects.

The electronic state of the SWCNTs changes when molecules are encapsulated in them, that is 'local bandgap engineering'.[47] For example, from determination of the electronic state of nano-peapod Gd@C$_{82}$@SWCNT by using STS at 5 K, it has been reported that the band gap before encapsulation is 0.43 eV but 0.17 eV after encapsulation.[47,48] Since the π orbital protruding inside the SWCNT is spatially close to the π orbital of the fullerene and strongly interacts with it, the electronic state of the outer SWCNT and the band gap change.[48–50] Therefore, it is possible to modulate the electronic state of SWCNTs with nanometer spatial resolution via encapsulation. In fact, ambipolar field effect transistor (FETs) using the electronic state of Gd@C$_{82}$@SWCNT have been reported.[51] The bandgap is reduced by the inclusion of Gd@C$_{82}$, and p- and n-type electronic states become accessible by controlling the gate voltage.

In order to characterize the electronic configuration of the SWCNT with a TbPc$_2$ molecule, we performed STM on a Au(111)
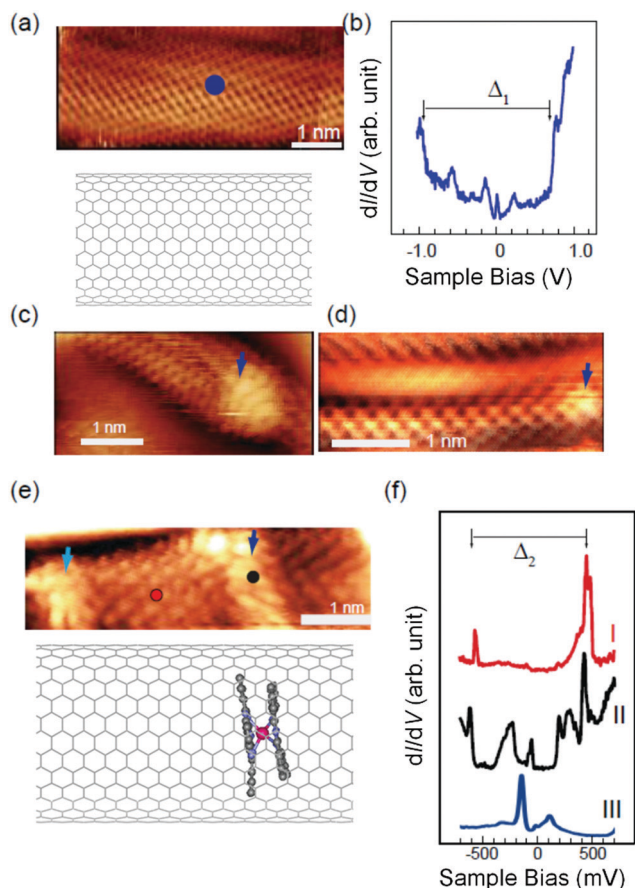
This journal is © The Royal Society of Chemistry 2021

J. Mater. Chem. C, 2021, **9**, 10697–10704 | **10701**

Fig. 5 (a) STM image and (b) STS spectra of empty SWCNT. (c) and (d) STM images of TbPc$_2$@SWCNT. (e) STM image showing empty (red) and filled (black) regions. (f) Comparative STS spectra measured at the red and black points in (e).

surface using a cryogenic STM setup. We observed the surface of the SWCNT with atomic scale resolution. Even for identical SWCNTs, one area showed a perfect periodic atom arrangement without disturbances, and the other area showed belt-like protrusions which disturbs the regular periodic structure. A topographical image for an area showing perfect periodicity is shown in Fig. 5(a) together with an STS spectrum obtained at the position of the blue circle in the topographical image shown in Fig. 5(b). The topographical image showed a periodic pattern and lattice size identical to those in our previous report.[52] In the STS spectrum, little change was observed even at other positions on the surface in Fig. 5(a). In Fig. 5(b), at both the occupied and unoccupied positions, indicated by arrows, there were staircase-like increases in the conductance, which are characteristic of van Hove singularities (VHS) and originate from the two-dimensional band structure of the CNT.[47]

At different parts of the SWCNTs, we observed protruded areas, which appear like nodules on the tube. The protrusion often had an inner structure which looked like a short belt running perpendicular to the long axis of the SWCNT. Examples of areas with the nodule-like protrusions are shown in Fig. 5(c) and (d). The bright regions are marked by arrows in all figures, which are ~ 0.2 Å protruded from the rest of the

SWCNT surface. However, there are reports where standing wave features are observed at the end of the SWCNT, which are caused by the forward wave and the backward wave scattered at the cap end.[52] Thus, to avoid any confusion, we concentrated on the protrusions in the middle of the tube. The density and the height were considerably different from those of the adsorbates or the defects of the SWCNT. In Fig. 5(c), the protrusion at the arrow had a striped pattern in which the stripes were separated by 2 Å. Note that this feature is not located at the end of the tube, although the right-hand side of the protrusion seems slightly narrow due to the imaging conditions. In Fig. 5(d), a clear atomic structure with a regular periodicity and the disturbance at the protrusion position in the right end were observed. In the magnified image of Fig. 5(e), two areas were protruded sandwiching a pristine region in the middle. There were clear inner structures with spacings similar to those of the SWCNT despite being distorted. We believe that they represent the position of the TbPc$_2$ molecules inside the SWCNT.

The STS spectra measured at the red and black positions of Fig. 5(e) are shown in Fig. 5(f). Plot I have two significant features, which are VHS pairs. The red mark is separated ~ 1 nm from the TbPc$_2$ positions. Thus, the effects of the encapsulated TbPc$_2$ are extended at least this far. On the other hand, plot II in Fig. 5(f) contains not only a VHS pair (Δ_2) but also several features between them. Those features are caused by the hybridization between the electronic states of the TbPc$_2$ molecule and the SWCNTs. The STS of the TbPc$_2$ molecule adsorbed on Au(111) surface, which is illustrated as plot III in Fig. 5(f) as a reference, has been reported by our group.[53] The two features straddling the Fermi level correspond to the highest occupied molecular orbital (HOMO) and lowest unoccupied molecular orbital (LUMO) from the π orbital of the Pc ligand. These two features can split in different chemical environments even for a single molecule, and this has been shown to occur for a TbPc$_2$ molecular film. The model of the adsorption for the TbPc$_2$ molecule inside the SWCNT tube illustrated in Fig. 5(e) shows the asymmetric potential from the substrate of the inner wall of the tube. Therefore, the appearance of split features can be explained by the potential difference among the TbPc$_2$ molecules. Since it is uncertain that the SWCNTs in Fig. 5a and e have the same chirality, it is highly possible that their original DOSs are different. Therefore, a simple comparison is not possible. In other words, the chirality of the SWCNTs must be the same for quantitative experimental investigation. On the other hand, from the information in Fig. 5e and f, it is clear that the DOSs between the part with TbPc$_2$ and the part without it are different, and the electron transport characteristics of SWCNTs can be controlled by encapsulating TbPc$_2$. Thus, it is thought that there are electronic interactions between TbPc$_2$ and SWCNT in the TbPc$_2$@SWCNT. It has been suggested that the electron correlation between TbPc$_2$ and SWCNT can affect the electronic transport properties and/or electromagnetic properties.[36,40,54]

Conclusions

We encapsulated neutral TbPc$_2$ molecules in SWCNTs by using a capillary method and confirmed the encapsulation by using

10702 | *J. Mater. Chem. C*, 2021, **9**, 10697–10704

This journal is © The Royal Society of Chemistry 2021

TEM, STEM, and EDX spectrometry. This is the first report of $TbPc_2$@SWCNT. However, the one-dimensional chain stacking of $TbPc_2$ was not confirmed. It is thought that there are small regions of stacking inside the one-dimensional nano space of SWCNT. $TbPc_2$ has a diameter size of about 2 nm and has a relatively weak affinity for SWCNTs due to its π-conjugated planar structure. Therefore, it does not encapsulate efficiently in one-dimensional stacks in a SWCNT. The frequency dependence due to $TbPc_2$ was shown by using ac magnetic susceptibility measurements, and the activation energy barrier U_{eff} and pre-exponential factor τ_0 estimated from the Arrhenius plot created from the peak top of the imaginary component were determined to be 430 cm^{-1} and 2.9×10^{-10} s, respectively. The values are consistent with those of pristine $TbPc_2$, suggesting that $TbPc_2$ retains its magnetic properties even in SWCNTs. From this result, it was determined that $TbPc_2$ was in a diluted state in SWCNT. On the other hand, the magnetic hysteresis temperature did not improve after encapsulation, which is because $TbPc_2$ molecules are not stacked in a one-dimensional chain structure. In addition, from the STM/STS, it was determined that there were electronic interactions between the $TbPc_2$ molecules and SWCNTs in $TbPc_2$@SWCNT. Since bandgap modulation was observed due to the encapsulation of $TbPc_2$ in the SWCNTs, these materials should be useful in field effect transistors. We are currently working to improve the encapsulation rate of $TbPc_2$ and the one-dimensional chain structure, which should improve the SMMs properties *via* 'local bandgap engineering'. Our work may pave the way for the construction of SMM–CNT hybrid materials, including SMM–CNT spin valves.

Author contributions

M. Y. conceived the idea, coordinated the experimental works. J. S., R. N., Y. K., and T. S. prepared the materials. J. S. and R. N. developed the experimental methodology, the characterization, and analysed the data. J. S., R. N. and K. K. carried out the magnetic measurements and analysed data. F. A. and T. K. carried out the scanning probe microscope measurements and analysed data. K. K., T. K., R. N., B. K. B. and M. Y. discussed the data and wrote the original manuscript. All the authors read and commented on the manuscript.

Conflicts of interest

There are no conflicts to declare.

Acknowledgements

References

1 M. N. Leuenberger and D. Loss, *Nature*, 2001, **410**, 789–793.

2 F. Troiani, A. Ghirri, M. Affronte, S. Carretta, P. Santini, G. Amoretti, S. Piligkos, G. Timco and R. E. P. Winpenny, *Phys. Rev. Lett.*, 2005, **94**, 207208.

3 G. Aromí, D. Aguilà, P. Gamez, F. Luis and O. Roubeau, *Chem. Soc. Rev.*, 2012, **41**, 537–546.

4 F. Luis, A. Repollés, M. J. Martínez-Pérez, D. Aguilà, O. Roubeau, D. Zueco, P. J. Alonso, M. Evangelisti, A. Camón, J. Sesé, L. A. Barrios and G. Aromí, *Phys. Rev. Lett.*, 2011, **107**, 117203.

5 J. Bartolomée, F. Luis and J. F. Fernández, *Molecular magnets: physics and applications*, Springer-Verlag/Sci-Tech/Trade, 2013.

6 R. Vincent, S. Klyatskaya, M. Ruben, W. Wernsdorfer and F. Balestro, *Nature*, 2012, **488**, 357–360.

7 F. Troiani and M. Affronte, *Chem. Soc. Rev.*, 2011, **40**, 3119–3129.

8 R. Sessoli, D. Gatteschi, A. Caneschi and M. A. Novak, *Nature*, 1993, **365**, 141–143.

9 J. R. Friedman, M. P. Sarachik, J. Tejada and R. Ziolo, *Phys. Rev. Lett.*, 1996, **76**, 3830–3833.

10 W. Wernsdorfer and R. Sessoli, *Science*, 1995, **16**, 1315–1325.

11 F. Luis, J. Bartolomé, J. F. Fernández, J. Tejada, J. M. Hernández, X. X. Zhang and R. Ziolo, *Phys. Rev. B: Condens. Matter Mater. Phys.*, 1997, **55**, 11448–11456.

12 E. Moreno-Pineda, M. Damjanović, O. Fuhr, W. Wernsdorfer and M. Ruben, *Angew. Chem., Int. Ed.*, 2017, **56**, 9915–9919.

13 G. A. Timco, S. Carretta, F. Troiani, F. Tuna, R. J. Pritchard, C. A. Muryn, E. J. L. McInnes, A. Ghirri, A. Candini, P. Santini, G. Amoretti, M. Affronte and R. E. P. Winpenny, *Nat. Nanotechnol.*, 2009, **4**, 173–178.

14 C. J. Wedge, G. A. Timco, E. T. Spielberg, R. E. George, F. Tuna, S. Rigby, E. J. L. Mcinnes, R. E. P. Winpenny, S. J. Blundell and A. Ardavan, *Phys. Rev. Lett.*, 2012, 107204.

15 D. Gatteschi and R. Sessoli, *Angew. Chem., Int. Ed.*, 2003, **42**, 268–297.

16 N. Ishikawa, M. Sugita, T. Ishikawa, S. Y. Koshihara and Y. Kaizu, *J. Am. Chem. Soc.*, 2003, **125**, 8694–8695.

17 F. S. Guo, B. M. Day, Y. C. Chen, M. L. Tong, A. Mansikkamäki and R. A. Layfield, *Science*, 2018, **362**, 1400–1403.

18 C. J. Milios and R. E. P. Winpenny, *Struct. Bonding*, 2015, **164**, 1–110.

19 C. Benelli and D. Gatteschi, *Introduction to molecular magnetism: from transition metals to lanthanides*, Wiley, 2015.

This journal is © The Royal Society of Chemistry 2021

J. Mater. Chem. C, 2021, **9**, 10697–10704 | **10703**

20 N. Ishikawa, M. Sugita and W. Wernsdorfer, *Angew. Chem., Int. Ed.*, 2005, **44**, 2931–2935.

21 N. Ishikawa, M. Sugita, N. Tanaka, T. Ishikawa, S. Y. Koshihara and Y. Kaizu, *Inorg. Chem.*, 2004, **43**, 5498–5500.

22 W. Wernsdorfer, N. Aliaga-Alcalde, D. N. Hendrickson and G. Christou, *Nature*, 2002, **416**, 406–409.

23 K. Katoh, S. Yamashita, N. Yasuda, Y. Kitagawa, B. K. Breedlove, Y. Nakazawa and M. Yamashita, *Angew. Chem., Int. Ed.*, 2018, **57**, 9262–9267.

24 T. Yamabayashi, K. Katoh, B. Breedlove and M. Yamashita, *Molecules*, 2017, **22**, 999.

25 S. Iijima, *Nature*, 1991, **354**, 56–58.

26 M. Menon and D. Srivastava, *Phys. Rev. Lett.*, 1997, **79**, 4453–4456.

27 S. J. Tans, A. R. M. Verschueren and C. Dekker, *Nature*, 1998, **393**, 49–52.

28 V. I. Preprint, S. W. Emmons and A. M. Leroi, *Nature*, 1999, **402**, 253–254.

29 W. Lu and C. M. Lieber, *Nat. Mater.*, 2007, **6**, 841–850.

30 P. M. Ajayan, T. W. Ebbesen, T. Ichihashi, S. Iijima, K. Tanigaki and H. Hiura, *Nature*, 1993, **362**, 522–525.

31 E. Dujardin, T. W. Ebbesen, H. Hiura and K. Tanigaki, *Science*, 1994, **265**, 1850–1852.

32 B. W. Smith, M. Monthioux and D. E. Luzzi, *Nature*, 1998, **396**, 323–324.

33 T. Pichler, H. Kuzmany, H. Kataura and Y. Achiba, *Phys. Rev. Lett.*, 2001, **87**, 267401.

34 S. Bandow, M. Takizawa, K. Hirahara, M. Yudasaka and S. Iijima, *Chem. Phys. Lett.*, 2001, **337**, 48–54.

35 R. Kitaura, N. Imazu, K. Kobayashi and H. Shinohara, *Nano Lett.*, 2008, **8**, 693–699.

36 L. Bogani and W. Wernsdorfer, *Nat. Mater.*, 2008, **7**, 179–186.

37 M. del Carmen Giménez-López, F. Moro, A. La Torre, C. J. Gómez-García, P. D. Brown, J. van Slageren and A. N. Khlobystov, *Nat. Commun.*, 2011, **2**, 407.

38 R. Nakanishi, M. Yatoo, K. Katoh, B. Breedlove and M. Yamashita, *Materials*, 2017, **10**, 7.

39 S. Kyatskaya, J. R. G. Mascarós, L. Bogani, F. Hennrich, M. Kappes, W. Wernsdorfer and M. Ruben, *J. Am. Chem. Soc.*, 2009, **131**, 15143–15151.

40 M. Urdampilleta, S. Klyatskaya, J. P. Cleuziou, M. Ruben and W. Wernsdorfer, *Nat. Mater.*, 2011, **10**, 502–506.

41 R. Nakanishi, J. Satoh, K. Katoh, H. Zhang, B. K. Breedlove, M. Nishijima, Y. Nakanishi, H. Omachi, H. Shinohara and M. Yamashita, *J. Am. Chem. Soc.*, 2018, **140**, 10955–10959.

42 K. Katoh, Y. Yoshida, M. Yamashita, H. Miyasaka, B. K. Breedlove, T. Kajiwara, S. Takaishi, N. Ishikawa, H. Isshiki, F. Z. Yan, T. Komeda, M. Yamagishi and J. Takeya, *J. Am. Chem. Soc.*, 2009, **131**, 9967–9976.

43 R. Weiss and J. Fischer, *The Porphyrin Handbook*, Elsevier, 2003, pp. 171–246.

44 T. Saito, S. Ohshima, T. Okazaki, S. Ohmori, M. Yumura and S. Iijima, *J. Nanosci. Nanotechnol.*, 2008, **8**, 6153–6157.

45 T. Saito, W. C. Xu, S. Ohshima, H. Ago, M. Yumura and S. Iijima, *J. Phys. Chem. B*, 2006, **110**, 5849–5853.

46 Y. Li, T. Wang, H. Meng, C. Zhao, M. Nie, L. Jiang and C. Wang, *Dalton Trans.*, 2016, **45**, 19226–19229.

47 J. Lee, H. Kim, S. J. Kahng, G. Kim, Y. W. Son, J. Ihm, H. Kato, Z. W. Wang, T. Okazaki, H. Shinohara and Y. Kuk, *Nature*, 2002, **415**, 1005–1008.

48 D. J. Hornbaker, S. J. Kahng, S. Misra, B. W. Smith, A. T. Johnson, E. J. Mele, D. E. Luzzi and A. Yazdani, *Science*, 2002, **295**, 828–831.

49 Y. Cho, S. Han, G. Kim, H. Lee and J. Ihm, *Phys. Rev. Lett.*, 2003, **90**, 106402.

50 C. L. Kane, E. J. Mele, A. T. Johnson, D. E. Luzzi, B. W. Smith, D. J. Hornbaker and A. Yazdani, *Phys. Rev. B: Condens. Matter Mater. Phys.*, 2002, **66**, 235423.

51 T. Shimada, T. Okazaki, R. Taniguchi, T. Sugai, H. Shinohara, K. Suenaga, Y. Ohno, S. Mizuno, S. Kishimoto and T. Mizutani, *Appl. Phys. Lett.*, 2002, **81**, 4067–4069.

52 M. Furuhashi and T. Komeda, *Phys. Rev. Lett.*, 2008, **101**, 185503.

53 T. Komeda, H. Isshiki, J. Liu, K. Katoh and M. Yamashita, *ACS Nano*, 2014, **8**, 4866–4875.

54 M. Yamashita, *Bull. Chem. Soc. Jpn.*, 2021, **94**, 209–264.

10704 | *J. Mater. Chem. C*, 2021, **9**, 10697–10704

This journal is © The Royal Society of Chemistry 2021